A New Class of Devices: Magnetic Gear Differentials for Vehicle Drivetrains

This article has been accepted for publication in IEEE Transactions on Transportation Electrification. This is the author's version which has not been fully edited and content may change prior to final publication. Citation information: DOI 10.1109/TTE.2022.3208628

A New Class of Devices: Magnetic Gear Differentials for Vehicle Drivetrains

Mattia Filippini*, Riccardo Torchio*, *Member, IEEE*, Piergiorgio Alotto*, *Senior Member, IEEE*, Elvio Bonisoli‡, Luca Dimauro‡, Maurizio Repetto†

***Abstract*—Mechanical differentials are essential drivetrain components of automobiles and other wheeled vehicles, allowing the outer drive wheel to rotate faster than the inner drive wheel during turns. This paper presents a comprehensive description of a novel and recently patented alternative based on magnetic gears, which achieves the same functionality while providing distinctive advantages such as reduced maintenance, absence of lubrication, high efficiency. The paper describes the operation principle of such magnetic gear differential and two alternative constructive options, provides a dynamic model which allows the study of the device in driving conditions, presents a description of a prototype and validates finite element simulations with experimental results.**

***Index Terms*—Magnetic Gears, Magnetic Differential, Magnetic Drivetrain, Magnetic Transmission**

NOMENCLATURE MECHANICAL SYMBOLS

MG	Magnetic gear.
MD	Magnetic differential.
MG1, MG2	The two MGs used in an MD.
MDA, MDB	Magnetic differential type A and B.
P_i	Inner rotor pole pairs.
P_o	Outer rotor pole pairs.
n_s	Ferromagnetic poles of middle rotor.
T_M	Maximum MG torque on the outer rotor.
θ_e, θ_{e1}, θ_{e2}	Load angles of MG, MG1, MG2.
θ_i, ω_i, T_i	Inner rotor angle, speed, external torque.
θ_o, ω_o, T_o	Outer rotor angle, speed, external torque.
θ_s, ω_s, T_s	Middle rotor angle, speed, external torque.
ω_{o1}, ω_{o2}	Output wheels speed in MDA.
ω_{s1}, ω_{s2}	Output wheels speed in MDB.
J_i*, b_i*	MG inner rotor inertia and damping.
J_o*, b_o*	MG outer rotor inertia and damping.
J_s*, b_s*	MG middle rotor inertia and damping.
J_i, b_i	MD inner rotor inertia and damping.
J_{o1}, J_{o2}	MDA wheels rotor inertia.
b_{o1}, b_{o2}	MDA wheels rotor damping.
J_s, b_s	MDA interconnected (middle) rotors inertia and damping.
J_{s1}, J_{s2}	MDB wheels rotor inertia.
b_{s1},b_{s2}	MDB wheels rotor damping.
J_o, b_o	MDB interconnected (outer) rotors inertia and damping.
T_{o1}, T_{o2}	MDA External wheels torques.
T_{s1}, T_{s2}	MDB External wheels torques.
Y_{ij}^A	MDA transfer function between input i and output j.
Y_{ij}^B	MDB transfer function between input i and output j.
M1	Prototype traction motor.
M2	Prototype differential control motor.
M3, M4	Prototype wheels motors.
G	Nominal gear ratio, with fixed interconnected rotor.
G_1, G_2	Input-output gear ratios of MG1 and MG2.
G_i	Mechanical ratio coupling source.
G_o	Mechanical ratio coupling outer rotor.
G_{oo}	Mechanical ratio coupling interconnection.

Manuscript received –; revised –; accepted –. Date of publication –; date of current version–. The review of this paper was coordinated by – (*Corresponding author: Mattia Filippini*).

Mattia Filippini, Riccardo Torchio and Piergiorgio Alotto are with the Department of Industrial Engineering, Università degli Studi di Padova, via Gradenigo 6/a, 35131 Padova, Italy (e-mail: mattia.filippini@unipd.it; riccardo.torchio@unipd.it; piergiorgio.alotto@unipd.it).

Elvio Bonisoli and Luca Dimauro are with DIMEAS – Politecnico di Torino, Corso Duca degli Abruzzi, 24, 10129, Torino, Italy (e-mail: elvio.bonisoli@polito.it; luca.dimauro@polito.it).

Maurizio Repetto is with DENERG – Politecnico di Torino, Corso Duca degli Abruzzi, 24, 10129, Torino, Italy (e-mail: maurizio.repetto@polito.it).

I. INTRODUCTION

Differentials are particular gear trains with one input (the traction motor) and two outputs (the wheels), allowing the outputs to have different rotational speeds [1]. These devices are normally used in vehicles and allow for transmitting the torque in steering conditions when the wheels have to rotate at different speeds. Such gear trains, ubiquitously adopted in automobiles, also electrical ones [2], are mechanical devices, based on the combination of lubricated gears. Despite their simplicity, they suffers from intrinsic drawbacks, such as friction, noise, vibrations, need for lubricant replacement, and relatively low efficiency [3]. These factors limit the gears' life and could lead to premature failures if not monitored.

Magnetic gears are good candidates to replace their mechanical counterparts since the power transfer is contact-less [4]. The structure of a radial flux coaxial magnetic gear is shown in Fig. 1: it consists of three coaxial rotors with permanent magnets (PMs) mounted on the inner and the outer ones, while the middle rotor consists of a set of ferromagnetic poles. P_i is the number of inner magnetic pole pairs, P_o is the number of outer magnetic pole pairs and n_s is the number of ferromagnetic poles. If $n_s = P_i + P_o$, the middle rotor acts as a field modulator, allowing for transmitting a constant torque (if ripple is neglected) between the inner and outer rotors, rotating with speed ratio $\frac{P_o}{P_i}$ (the reader is referred to [3] for further details on the operating principle). The contact-less nature of the electromagnetic interaction results in almost

This article has been accepted for publication in IEEE Transactions on Transportation Electrification. This is the author's version which has not been fully edited and content may change prior to final publication. Citation information: DOI 10.1109/TTE.2022.3208628

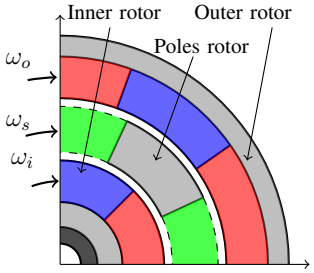

Fig. 1: One fourth of a typical magnetic gear. Materials: magnets (blue-red), ferromagnetic iron (grey), polymer (green), shaft (black).

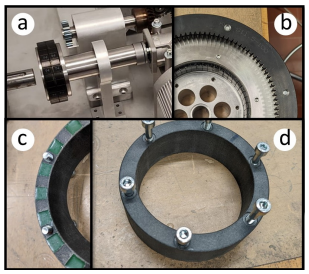

Fig. 2: Components of the prototyped magnetic gear: (a) inner rotor, (b) outer rotor, (c) poles rotor back and (d) poles rotor front.

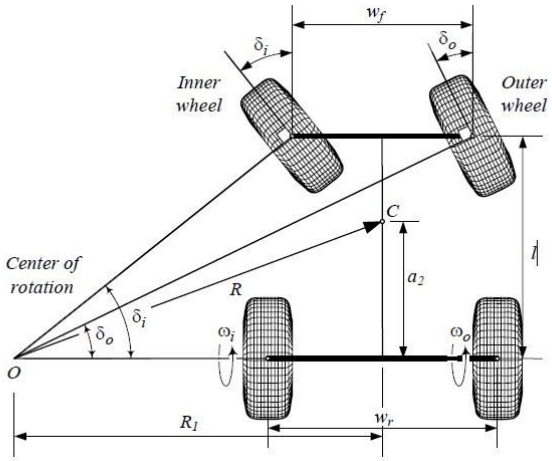

Fig. 3: Ackerman's steering geometry. The cornering radii are different from inner to outer wheels, thus a differential device is needed to avoid slip between tire and ground.

noiseless devices that do not require lubrication (except for the bearings), achieve high efficiencies and are potentially maintenance-free. Another aspect that is worth considering is the intrinsic over-slip operation offered by the contact-less transmission: instead of designing clutches to avoid torque peaks to be transferred by the gearbox, the magnetic gear simply slips when the torque limit is reached. This can be a great advantage for the optimization of space, weight and complexity of an automotive drive-train. On the contrary, the absence of direct contact directly impacts the torsional stiffness of the coupling [5], which is much lower than the one of mechanical transmissions (ideally infinite).

Several topologies appeared in the last decades with the main goal of increasing the torque density and the possibility of obtaining devices with variable gear ratio has been considered in several works [6], [7], [8], [9].

For a typical magnetic gear, shown in Figs.1 and 2, the rotor speed relationship in stationary conditions reads [7], [10]:

$$\omega_o = -\frac{P_i}{n_s - P_i}\omega_i + \frac{n_s}{n_s - P_i}\omega_s \tag{1}$$

where ω_o, ω_i, and ω_s are the speed of outer, inner, and poles rotor, respectively.

Magnetic gears are synchronous machines, thus the load speed ω_o in stationary conditions is defined once ω_s and ω_i are fixed; this means that slip cannot occur during the nominal operation (otherwise (1) will not hold true). Thus, magnetic gears would be unsuited for a vehicle differential application with a single motor where an asynchronous operation is requested. A simple solution adopting magnetic transmissions could be obtained with two magnetic gears with fixed ratio and two independent electrical motors or geared motors [11], i.e. an electric differential as in [12], [13], but this solution is costly. Some mechanical setups can also be used to obtain a variable gear ratio, but these solutions are rather complex and require maintenance [14] or achieve only discrete variations of gear ratios [15].

In this paper, two novel magnetic differential topologies are proposed as additional layouts to the ones presented in [16]: the basic drivetrain is composed of two magnetic gears, one mechanical gear, one power source (electrical or thermal). These configurations are also briefly described in [17], where the main features are outlined. In the proposed solution the output shafts speeds are equal when the loads are equal, while the magnetic gears provide torque to asynchronously-rotating shafts when the loads are speed-unbalanced.

In the literature, some works have applied standard control theory to magnetic transmissions in order to study the dynamics and to prevent the asynchronous operation [18], [19], [20]. In this paper, the proposed configuration is studied through the same control theory approaches in order to assess the stability of the system of dynamic equations.

The paper is organized as follows: Sec. II introduces the concept of differential and its role in drivetrains. In Sec. III, two configurations of magnetic differential are proposed and their relative advantages are described. Sec. IV presents a simplified analysis of the device, with a focus on the control theory perspective and a simplified test case where the differential operation is verified.

In the second part of the paper, i.e. Secs. V to VIII, a prototype of one of the proposed topologies is designed in detail, with the aid of numerical models validated through measurements. In these sections, all aspects related to construction, assembly, and validation are discussed. Finally, Sec. IX provides some comments concerning the manufacturing issues of magnetic gears and magnetic differentials.

II. Vehicle Dynamics Steering

Fig. 3 represents the Ackermann steering geometry [21]. Generally, when a vehicle is steering, each wheel has a certain radius referred to the center of rotation, and all radii are different. Since the wheels are supposed to have the same geometry, the rotational speed of the wheels should be different (in the hypothesis of equal negligible slip VS ground) since the distance to travel is different, and this is normally achieved with differential gearboxes.

This article has been accepted for publication in IEEE Transactions on Transportation Electrification. This is the author's version which has not been fully edited and content may change prior to final publication. Citation information: DOI 10.1109/TTE.2022.3208628

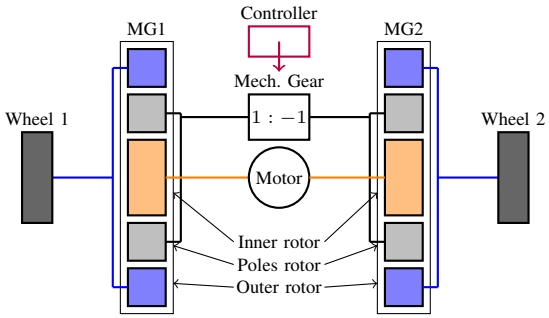

Fig. 4: Cross section of the proposed MDA topology. A mechanical gear with ratio $k = -1$ is adopted for the counter rotation of the iron poles rotors.

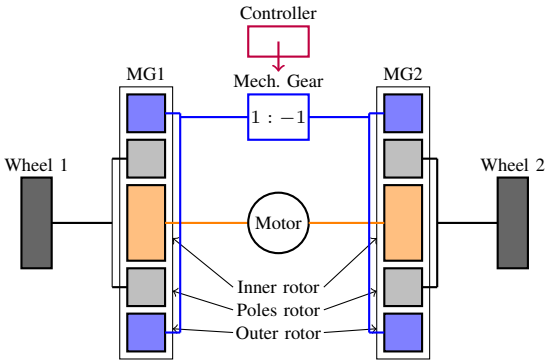

Fig. 5: Cross section of the MDB topology. A mechanical gear with ratio $k = -1$ is adopted for the counter rotation of the outer rotors.

If the wheels are connected through a rigid axle, the torque and speed expressions are:

$$\begin{cases} T_{drive} = T_{outer} + T_{inner} \\ \omega_{drive} = \omega_{outer} = \omega_{inner} \end{cases} \tag{2}$$

where T_{inner}, T_{outer}, ω_{inner}, ω_{outer}, are torques and rotational speeds of the inner and outer wheels referred to the center of rotation, while T_{drive} and ω_{drive} are the ones of the traction motor. For a rigid axle, the inner wheel will have a positive slip while the outer wheel have a lower or even negative slip. This leads to a larger force on the inner wheel that counteracts the vehicle steering motion. The differential is used to overcome these drawbacks. The simplest differential type is the open one. For this device the speed and torque equations holds:

$$\begin{cases} 0.5 \cdot T_{drive} = T_{outer} = T_{inner} \\ \omega_{drive} = 0.5 \cdot (\omega_{outer} + \omega_{inner}) \end{cases} \tag{3}$$

Thus, torques on the two wheels are equal and are not dependent on the rotational speeds. The maximum wheels speed ratio depends on the vehicle steering capability. For example, if R_{steer}^{min} is the minimum outer steering radius and w is the rear axle wheel to wheel distance, by setting $R_{steer}^{min} = 5$ m and $w = 2$ m, the maximum ratio between outer and inner wheel speed is

$$\Psi^{max} = \frac{R_{steer}^{min}}{R_{steer}^{min} - w} = \frac{5}{3} = 1.67$$

The proposed magnetic differential will have the same mechanical characteristic of (3) in its basic implementation.

III. Proposed Configurations

As previously stated, two magnetic differential (MD) solutions are considered although only one will be prototyped. The two magnetic differential solutions are shown in Fig. 4 and Fig. 5, and these will be referred as type A (MDA) and type B (MDB). Both configurations adopt two coaxial magnetic gears MG1 and MG2 and the gears inner rotors (high speed) are connected together and to a power source (e.g. internal combustion engine). A similar structure could be obtained with axial flux MGs [22] or other structures [23] but because of the higher mechanical complexity these solutions will not be discussed in this paper. The low speed outer rotors of the magnetic gears are connected to the wheels and the iron poles rotors are connected together through a classical mechanical gearbox with gear ratio $G_m = -1$ in MDA. Instead, in MDB, the poles rotors are connected to the wheels while the outer rotors are connected to the mechanical gearbox. The connection of poles rotors and gearbox in MDA will be referred to as *interconnected rotor* (conversely, in MDB the *interconnected rotor* consists of the outer rotors plus the mechanical gearbox). It is worth highlighting that the layouts of Figs. 4 and 5 are schematic representations of the assembly: e.g. the traction motor in these figures is a 2-axis one and is coaxial with the gears, while the torque topology is not specified in the scheme. Different layouts, e.g. where the traction motor is in a different position/orientation or with a specific mechanical system coupling with ratio -1 (e.g. a planetary gear set or a hydro-static coupling), are completely equivalent and the easiest manufacturing solution can be adopted.

Recalling Sec. II, the role of the differential is to deliver torque from the power source to the two rotating wheels with different speeds. In MDA, during the normal operation of the drivetrain, i.e. when the vehicle is moving along a straight path, the load torques and wheels speeds are balanced. This means that equal torques are developed on the iron poles rotor and because of the mechanical coupling the global torque acting on the rotor is nil. In this condition, the *interconnected rotor* is still, thus $\omega_s = 0$ in (1) and this means that both MG1 and MG2 have gear ratios $G_1 = G_2 = G$, where G_1 and G_2 are the input-output gear ratios $\frac{\omega_i}{\omega_o}$ of MG1 and MG2, respectively, and $G = \frac{P_o}{P_i}$ is the nominal ratio. This is no longer true in the case of unbalanced loads, e.g. when the vehicle steers. The load unbalance results in a poles rotor unbalance, thus the *interconnected rotor* will rotate at speed ω given by the new mechanical equilibrium. Because of the mechanical coupling, in MG1 $\omega_s = \omega$ while in MG2 $\omega_s = -\omega$, thus through (1) MG1 and MG2 will have different gear ratios, e.g. $G_1 < G < G_2$: the result is indeed a differential operation of the transmission. According to (1), if ω_o is positive and tends to decrease because the vehicle is steering, ω_s has to increase if ω_i is kept constant. In turn, for the other gear ω_s tends to

decrease and ω_o tends to increase. The combined action gives the steering capability. The same principle applies to the MDB topology, substituting ω_o with ω_s and setting the nominal gear ratio to $G = \frac{n_s}{P_i}$.

Torques developed on the three rotors of a magnetic gear depend only on the load angle θ_e if losses and cogging torque are neglected. For the MDB case, the load angles of MG1 and MG2 are θ_{e1} and θ_{e2}:

$$\begin{cases} \theta_{e1} = P_o\theta_o + P_i\theta_i - n_s\theta_{s1} \\ \theta_{e2} = -P_o\theta_o + P_i\theta_i - n_s\theta_{s2} \end{cases} \tag{4}$$

where the same notation of (1) has been adopted, i.e. θ_i, θ_o, θ_{s1} and θ_{s2} are the inner rotor position (equal for MG1 and MG2), *interconnected rotor* position (opposite for MG1 and MG2), and wheels positions. In steady state operation, the load angles θ_{e1} and θ_{e2} are stationary, thus differentiating the rotational speed equations we obtain:

$$P_o\omega_o + P_i\omega_i - n_s\omega_{s1} = \frac{d\theta_{e1}}{dt} = 0 \tag{5}$$

$$-P_o\omega_o + P_i\omega_i - n_s\omega_{s2} = \frac{d\theta_{e2}}{dt} = 0 \tag{6}$$

In steady state cornering conditions, when $\omega_{s1} = k_{steer}\omega_{s2}$, the interconnected rotor speed is expressed as:

$$n_s(\omega_{s1} - \omega_{s2}) = n_s(k_{steer} - 1)\omega_{s2} = 2P_o\omega_o \tag{7}$$

The equation above also applies to the angles choosing the same angular reference for $s1$, $s2$, o:

$$n_s(\theta_{s1} - \theta_{s2}) = n_s(k_{steer} - 1)\theta_{s2} = 2P_o\theta_o \tag{8}$$

Substituting (8) in the last two of (4), the load angles in steady state cornering are:

$$\begin{cases} \theta_{e1} = P_o\theta_o + P_i\theta_i - n_s\theta_{s2} - 2P_o\theta_o \\ \theta_{e2} = -P_o\theta_o + P_i\theta_i - n_s\theta_{s2} \end{cases} \tag{9}$$

From (9), the load angles are equal for the two magnetic gears, thus the input torque from the inner rotor is equally distributed to the wheels, as in a mechanical open differential (see Sec. II). The same conclusion holds for the MDA topology.

As already mentioned, since a clutch is intrinsically included in a magnetic gear, some considerations are needed regarding the stability of the whole system (for example to handle the asynchronous operation when a gear torque capability is exceeded). The easiest method to control the device would be to adopt a second motor on the poles rotor that forces the appropriate speed according to the steering radius. This would allow to implement advanced control techniques [24], such as differential locking and torque vectoring. Since the wheels are coupled to the road, the interaction between wheels and road gives a natural steering capability limited by the maximum grip force. The motor controller connected to the mechanical gear could also be replaced by a cheaper mechanical brake that has to ensure stability. When for example the torque limit is reached on the wheels, the magnetic gears operation turns to asynchronous and the *interconnected rotor* speed in (1) tends to grow (since the wheels load is lost, the torque balance is now at much higher speed). The braking torque value is controlled through a proportional-integral (PI) regulator linked to the overload speed $\Delta\omega$ of the interconnected rotor referring to the fixed limit (from the design parameters and the maximum load unbalance the speed limit can be estimated).

It is worth noting that the mechanical gear has just the role of torque inverter and there are several solutions that can be used. Here the classical solution with 3 bevel gears have been chosen for its simplicity. Anyway, the key difference with a pure mechanical differential is that this component does not transmit power in nominal conditions, while in steering conditions the rotational speed is limited in the hypothesis of small slip. The component lifetime is therefore extended if compared to the standard differential operation and the conversion efficiency comes into play only during steering on a limited amount of power transferred between MG1 and MG2.

IV. Simplified Analysis

In this section, the dynamic model of the whole differential system is analyzed. These equations are useful to determine the relations between each input and output of the system and how the electro-mechanical parameters of each rotor affect the dynamic response of all the output speeds. This is a mandatory analysis that allows for comparing the magnetic differential performance with the one of the mechanical differential, where the system can be assumed as infinitely stiff.

The simplified analysis of the magnetic gear relies on the hypothesis of negligible torque ripple and unitary conversion efficiency. According to [6], the dynamic equations of the rotors of a single magnetic gear with maximum torque capability T_M (of the outer rotor) can be expressed as:

$$\begin{cases} J_i^* \frac{d^2\theta_i}{dt^2} + b_i^* \frac{d\theta_i}{dt} = T_i - \frac{P_i}{P_o} T_M \sin(P_o\theta_o + P_i\theta_i - n_s\theta_s) \\ J_o^* \frac{d^2\theta_o}{dt^2} + b_o^* \frac{d\theta_o}{dt} = T_o - T_M \sin(P_o\theta_o + P_i\theta_i - n_s\theta_s) \\ J_s^* \frac{d^2\theta_s}{dt^2} + b_s^* \frac{d\theta_s}{dt} = T_s + \frac{n_s}{P_o} T_M \sin(P_o\theta_o + P_i\theta_i - n_s\theta_s) \end{cases} \tag{10}$$

where J_i^*, J_o^* and J_s^* are the inner, outer and pole rotor inertia, b_i^*, b_o^* and b_s^* are the inner, outer and pole rotor damping coefficients and T_i, T_o and T_s are the external torques applied, respectively. The approximation of torques related to the load angle through the $\sin$ function holds especially when the gear ratio is fractional, since the torque ripple is low.

A. Configuration A

In this configuration, (10) is extended with the equation set of a second magnetic gear. The argument of the $\sin$ function can be referred as load angle $\theta_e = P_o\theta_o + P_i\theta_i - n_s\theta_s$. The load angles of MG1 and MG2 in Fig. 4 are θ_{e1} and θ_{e2}, respectively. The dynamic set of equations of Fig. 4 is thus:

$$\begin{cases} J_i \frac{d^2\theta_i}{dt^2} + b_i \frac{d\theta_i}{dt} = T_i - \frac{P_i}{P_o} T_M (\sin\theta_{e1} + \sin\theta_{e2}) \\ J_{o1} \frac{d^2\theta_{o1}}{dt^2} + b_{o1} \frac{d\theta_{o1}}{dt} = T_{o1} - T_M \sin(\theta_{e1}) \\ J_{o2} \frac{d^2\theta_{o2}}{dt^2} + b_{o2} \frac{d\theta_{o2}}{dt} = T_{o2} - T_M \sin(\theta_{e2}) \\ J_s \frac{d^2\theta_s}{dt^2} + b_s \frac{d\theta_s}{dt} = T_s + \frac{n_s}{P_o} T_M (\sin\theta_{e1} - \sin\theta_{e2}) \\ \theta_{e1} = P_o\theta_{o1} + P_i\theta_i - n_s\theta_s \\ \theta_{e2} = P_o\theta_{o2} + P_i\theta_i + n_s\theta_s \end{cases} \tag{11}$$

where J_i, b_i and T_i are the inertia, damping and torque of the inner rotor in Fig. 4. J_s, b_s and T_s are the inertia, damping and torque of the whole *interconnected rotor*, J_{o1}, b_{o1}, T_{o1}, J_{o2}, b_{o2}, T_{o2} are the inertia, damping and torque of the two outer rotors in Fig. 4. The dynamic equation set in (11) is a multiple input multiple output model (MIMO), where the 4 inputs are the torques T_i, T_{o1}, T_{o2}, T_s and the outputs are the rotational speeds of the 4 rotors $\omega_i = \frac{d\theta_i}{dt}$, $\omega_{o1} = \frac{d\theta_{o1}}{dt}$, $\omega_{o2} = \frac{d\theta_{o2}}{dt}$ and $\omega_s = \frac{d\theta_s}{dt}$.

$$\begin{bmatrix} \omega_i \\ \omega_{o1} \\ \omega_{o2} \\ \omega_s \end{bmatrix} = \begin{bmatrix} Y_{11}^A & Y_{12}^A & Y_{13}^A & Y_{14}^A \\ Y_{21}^A & Y_{22}^A & Y_{23}^A & Y_{24}^A \\ Y_{31}^A & Y_{32}^A & Y_{33}^A & Y_{34}^A \\ Y_{41}^A & Y_{42}^A & Y_{43}^A & Y_{44}^A \end{bmatrix} \cdot \begin{bmatrix} T_i \\ T_{o1} \\ T_{o2} \\ T_s \end{bmatrix} \tag{12}$$

(12) shows the transfer function matrix, where Y_{ij} is the transfer function between the i^{th} output and the j^{th} input when all the other input torques are nil. Because of the $\sin$ functions, the system has to be linearized for the transfer function evaluation. In this paper, the model is linearized considering $\sin(x) \simeq x$, hypothesis which is verified when the load angles θ_{e1} and θ_{e2} are small.

B. Configuration B

With the same approach of Sec. IV-A, the dynamic set of equations of Fig. 5 is:

$$\begin{cases} J_i \frac{d^2\theta_i}{dt^2} + b_i \frac{d\theta_i}{dt} = T_i - \frac{P_i}{P_o} T_M (\sin\theta_{e1} + \sin\theta_{e2}) \\ J_{s1} \frac{d^2\theta_{s1}}{dt^2} + b_{s1} \frac{d\theta_{s1}}{dt} = T_{s1} + \frac{n_s}{P_o} T_M \sin(\theta_{e1}) \\ J_{s2} \frac{d^2\theta_{s2}}{dt^2} + b_{s2} \frac{d\theta_{s2}}{dt} = T_{s2} + \frac{n_s}{P_o} T_M \sin(\theta_{e2}) \\ J_s \frac{d^2\theta_o}{dt^2} + b_o \frac{d\theta_o}{dt} = T_s - T_M (\sin\theta_{e1} - \sin\theta_{e2}) \\ \theta_{e1} = P_o\theta_o + P_i\theta_i - n_s\theta_{s1} \\ \theta_{e2} = -P_o\theta_o + P_i\theta_i - n_s\theta_{s2} \end{cases} \tag{13}$$

where J_i, b_i and T_i are the inertia, damping and torque of the inner rotor in Fig. 5. J_o, b_o and T_o are the inertia, damping and torque of the whole *interconnected rotor*, J_{s1}, b_{s1}, T_{s1}, J_{s2}, b_{s2}, T_{s2} are the inertia, damping and torque of the two poles rotors in Fig. 5. As for the previous case, the dynamic equation set in (13) is a multiple input multiple output model (MIMO), where the 4 inputs are the torques T_i, T_{s1}, T_{s2}, T_o and the outputs are the rotational speeds of the 4 rotors $\omega_i = \frac{d\theta_i}{dt}$, $\omega_{o1} = \frac{d\theta_{o1}}{dt}$, $\omega_{o2} = \frac{d\theta_{o2}}{dt}$ and $\omega_s = \frac{d\theta_s}{dt}$.

$$\begin{bmatrix} \omega_i \\ \omega_{s1} \\ \omega_{s2} \\ \omega_o \end{bmatrix} = \begin{bmatrix} Y_{11}^B & Y_{12}^B & Y_{13}^B & Y_{14}^B \\ Y_{21}^B & Y_{22}^B & Y_{23}^B & Y_{24}^B \\ Y_{31}^B & Y_{32}^B & Y_{33}^B & Y_{34}^B \\ Y_{41}^B & Y_{42}^B & Y_{43}^B & Y_{44}^B \end{bmatrix} \cdot \begin{bmatrix} T_i \\ T_{s1} \\ T_{s2} \\ T_o \end{bmatrix} \tag{14}$$

Again, Y_{ij} is the transfer function between the i^{th} output and the j^{th} input when all the other inputs are nil, and the $\sin$ functions have to be linearized by setting $\sin(x) \simeq x$, hypothesis which is verified when the load angles θ_{e1} and θ_{e2} are small.

C. A Note on System Stability

System stability is one of the first concerns when dealing with dynamic systems. In this section, the bounded input bounded output (BIBO) stability will be proved for the linearized system in (12) and (14).

The following coefficients are adopted for the analysis of solution MDA:

$$\begin{cases} d_1 = J_i s^2 + b_i s \\ d_2 = J_{o1} s^2 + b_{o1} s \\ d_3 = J_{o2} s^2 + b_{o2} s \\ d_4 = J_s s^2 + b_s s \\ K_1 = P_i / P_o \\ K_2 = n_s / P_o \\ n_1 = P_i;\ \alpha_1 = K_1 T_M n_1 \\ n_2 = n_3 = P_o;\ \alpha_2 = T_M n_2;\ \alpha_3 = T_M n_2 \\ n_4 = P_s;\ \alpha_4 = K_2 T_M n_4 \end{cases} \tag{15}$$

With the same notation, for the configuration MDB, the set of parameters is:

$$\begin{cases} d_1 = J_i s^2 + b_i s \\ d_2 = J_{s1} s^2 + b_{s1} s \\ d_3 = J_{s2} s^2 + b_{s2} s \\ d_4 = J_o s^2 + b_o s \\ K_1 = P_i / P_o \\ K_2 = n_s / P_o \\ n_1 = P_i;\ \alpha_1 = K_1 T_M n_1 \\ n_2 = n_3 = n_s;\ \alpha_2 = T_M n_2;\ \alpha_3 = T_M n_3 \\ n_4 = P_o;\ \alpha_4 = K_2 T_M n_4 \end{cases} \tag{16}$$

Substituting (11) with the coefficients expressed in (15), and (16), (17), and (18) are obtained, respectively. The inverse of G can be written as $G^{-1} = adj(G)/det(G)$, where adj is the adjoint matrix and det is the determinant function. The system is BIBO stable if and only if an irreducible representation of the determinant has all negative real part roots. The determinant of G^A and G^B in (19) is a polynomial with degree 8. Through the symbolic expression of the matrix determinant it is not possible to find a factorized expression, but since all the coefficients p_i and r_i in (19) are always positive (sum of positive combinations of the terms J, b, P_i, P_o, n_s), all the roots of the determinant have negative real parts. This implies that both configurations MDA and MDB are BIBO stable.

D. Loop Without Road Transfer Function

In this section, the open loop operation of the MIMO system MDA is analyzed: the load of the two wheels are considered as independent, thus there is no closed loop between the input torques T_{o1} and T_{o2} and the relative shaft speeds ω_{o1} and ω_{o2} for MDA (T_{s1} and T_{s2} with relative shaft speeds ω_{s1} and ω_{s2} for MDB). The transfer function loop is still closed because in (11) the gears provide a torque that depends on the angular positions thus, when a load unbalance occurs, the new steady state equilibrium is defined by the damping coefficients of the MIMO system. The steady state responses have been obtained considering $\sin(x) \simeq x$, hypothesis that is verified when the load angles θ_{e1} and θ_{e2} are small. The expression

This article has been accepted for publication in IEEE Transactions on Transportation Electrification. This is the author's version which has not been fully edited and content may change prior to final publication. Citation information: DOI 10.1109/TTE.2022.3208628

$$\begin{bmatrix}\omega_i\\ \omega_{o1}\\ \omega_{o2}\\ \omega_s\end{bmatrix} = \frac{s}{1+sc}\underbrace{\begin{pmatrix} d_1+2\alpha_1 & \alpha_1 & \alpha_1 & 0\\ \alpha_2 & d_2+\alpha_2 & 0 & -\alpha_2\\ \alpha_3 & 0 & d_3+\alpha_3 & \alpha_3\\ 0 & -\alpha_4 & \alpha_4 & d_4+2\alpha_4\end{pmatrix}^{-1}}_{G^A} \cdot diag\begin{pmatrix} n_1\\ n_2\\ n_4\\ n_3\end{pmatrix} \cdot \begin{pmatrix} T_i\\ T_{o1}\\ T_{o2}\\ T_s\end{pmatrix} \tag{17}$$

$$\begin{bmatrix}\omega_i\\ \omega_{s1}\\ \omega_{s2}\\ \omega_o\end{bmatrix} = \frac{s}{1+sc}\underbrace{\begin{pmatrix} d_1+2\alpha_1 & -\alpha_1 & -\alpha_1 & 0\\ -\alpha_2 & d_2+\alpha_2 & 0 & -\alpha_2\\ -\alpha_3 & 0 & d_3+\alpha_3 & \alpha_3\\ 0 & -\alpha_4 & \alpha_4 & d_4+2\alpha_4\end{pmatrix}^{-1}}_{G^B} \cdot diag\begin{pmatrix} n_1\\ n_2\\ n_4\\ n_3\end{pmatrix} \cdot \begin{pmatrix} T_i\\ T_{s1}\\ T_{s2}\\ T_o\end{pmatrix} \tag{18}$$

$$\begin{aligned} det(G^A) &= p_0 + sp_1 + s^2p_2 + s^3p_3 + s^4p_4 + s^5p_5 + s^6p_6 + s^7p_6 + s^8p_8\\ det(G^B) &= r_0 + sr_1 + s^2r_2 + s^3r_3 + s^4r_4 + s^5r_5 + s^6r_6 + s^7r_6 + s^8r_8 \end{aligned} \tag{19}$$

TABLE I: MDA topology parameters adopted for the simplified simulation.

Parameter	Name	Value	Unit
J_i	Inner inertia	0.1	kg m^2
b_i	Inner damping	0.01	kg m/s
J_{o1}	Wheel 1 inertia	6	kg m^2
b_{o1}	Wheel 1 damping	0.6	kg m/s
J_{o2}	Wheel 2 inertia	6	kg m^2
b_{o2}	Wheel 2 damping	0.6	kg m/s
J_s	Poles inertia	0.1	kg m^2
b_s	Poles damping	0.3	kg m/s
J_{o2}	Wheel 2 inertia	6	kg m^2
T_M	Torque capability	100	Nm
P_i	Inner pole pairs	3	–
P_o	Outer pole pairs	10	–
n_s	Pole pieces	13	–
R_{wheel}	Wheel radius	0.25	m
$\lvert\omega_{i-max}\rvert$	Inner maximum speed	4000	rpm
$\lvert\omega_{s-max}\rvert$	Poles maximum speed	500	rpm
G	Magnetic differential gear ratio	$-10/3$	–

limits with $s \to 0$ are shown in (20)-(26) and (27)-(33) for MDA and MDB, respectively: these expressions are useful to compute the steady state transfer functions for all the input-output combinations of the differential, which in open loop depend on the mechanical properties of the system (this will be the principal working operation when the wheels are in no-load condition in Sec. VIII).

The parameters adopted for the simulation are shown in Table I; the wheels rotor inertia is much bigger than the other rotor's one since the vehicle mass m is included $J_{add} = mR^2_{wheel}$. With this hypothesis the mechanical model is simplified and an equivalent wheel load is used to model the whole vehicle load.

For the model test, an input torque step $T_i = 43$ Nm is applied to the input shaft. The input torque value can be modulated through a PI controller in order to avoid the gear asynchronous operation that can be triggered if during the dynamic transient the maximum torque capability T_M is exceeded. In this paper, the traction motor control with feedback is not implemented. At $t = 50$ s a load torque step $\Delta T = 10$ Nm is applied to the wheel 2 and this torque perturbation is removed at $t = 70$ s. Substituting in (20) and (23) the parameters of Table I, the steady state values

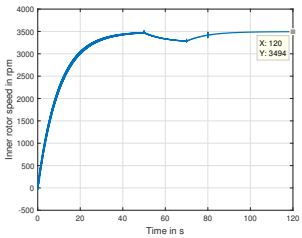

Fig. 6: Inner rotor speed ω_i with open loop.

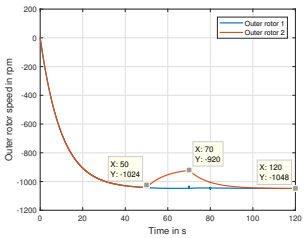

Fig. 7: Wheels speed ω_{o1} and ω_{o2}.

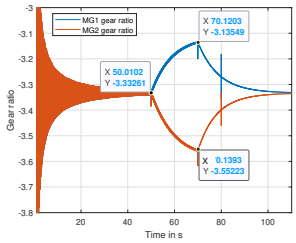

Fig. 8: Gear ratios of MG1 and MG2 VS time.

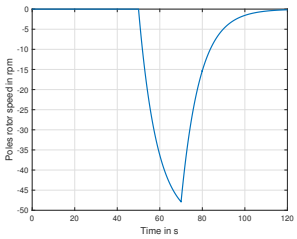

Fig. 9: Poles rotor speed ω_s with open loop.

are 81.9 rpm and 14 rpm, respectively, thus the expected inner speed in steady state is $\omega_i = 43 \cdot 81.9 = 3483$ rpm, while the speed deviation of the wheel 2 in steady state is $\Delta\omega_{o2} = 14 \cdot 10 = 140$ rpm.

Figs. 6 and 7 show the inner and wheels speed response. Because of the torque step, some oscillations are present before $t = 40$ s. In balanced conditions the estimated output speed is $\omega_{o1} = \omega_{o2} = 1045$ rpm and this value is in accordance to the steady state speed obtained from the simulation.

Fig. 8 shows the gears ratios of MG1 and MG2 while Fig. 9 shows the poles rotor speed. As explained in Sec. III, when the loads are balanced the poles are fixed since the torques applied by MG1 and MG2 cancel out. When the step torque is applied, the poles rotor start to rotate and the two gear ratios changes accordingly, while when the torque perturbation is removed the poles speed starts to decrease till zero.

In Fig. 10, the step responses of the MIMO system are

This article has been accepted for publication in IEEE Transactions on Transportation Electrification. This is the author's version which has not been fully edited and content may change prior to final publication. Citation information: DOI 10.1109/TTE.2022.3208628

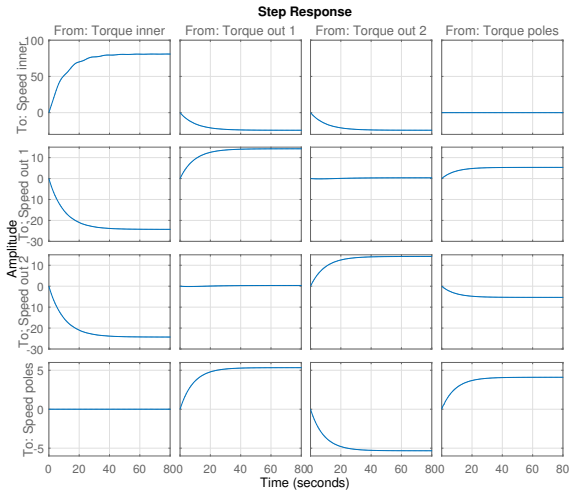

Fig. 10: Step response of the MIMO system for the set of parameters in Tab. I for the MDA topology.

depicted adopting again the hypothesis of linearized system with $\sin(x) \simeq x$. All the responses in the anti-diagonal are flat, meaning that the coupling of these in-out combinations is very weak.

E. Loop With Asynchronous Braking

When the torque limit of a magnetic gear is reached, the device starts the asynchronous operation. In this condition the average transmission torque is zero, thus if the traction motor injected torque is constant, the new equilibrium point is at a much higher speed, limited only by the inner mechanical damping. In the connection under investigation since all the three parts of the gear can rotate, three speeds have to be checked in order to detect the asynchronous operation.

In this paper, the traction motor torque control is a simple torque limiter based on the over-speed calculated referring to the maximum input shaft speed ω_{i-rpm}. The same strategy is adopted for the poles rotor since if only one wheel becomes asynchronous, the poles rotor new equilibrium speed can be higher than the mechanical limit ω_{s-max}. The speed error $\Delta\omega_s = |\omega_{s-max}| - |\omega_s|$ is set as input of a PI controller with outer upper limit $F_{max} = 0$ (antiwind-up system on the integrator has to be implemented). The PI output is the force F ($F <= 0$ always holds) applied to the brake that gives a resistive torque $T_R = 4sign(\omega_s)FR_{brake}k_r$ according to Fig. 11, where R_{brake} is the equivalent radius of the brake, the sign function $sign(x)$ is nil if $x = 0$ and the ratio k_r is the diameter ratio between the inputs bevels and the free bevel ($k_r > 1$ in Fig. 11). It is worth noting that the coefficient k_r and the brake radius R_{wheel} should be the highest possible since the braking toque has a linear relation with the term $R_{wheel}k_r$.

Fig. 12 shows the inner rotor speed with and without brake when a torque perturbation is added on wheel 2. As shown, the perturbation without brake forces the input shaft to a negative speed, while the shaft reaches its maximum speed when the torque step is removed. The new equilibrium point after the torque step is different from the one prior to the perturbation.

TABLE II: PI settings adopted.

Parameter	Name	Value
Kp_{pi-s}	Kp pole's rotor PI	1
Ki_{pi}	Ki pole's rotor PI	3
Kp_{pi-i}	Kp inner rotor PI	1
Ki_{pi-i}	Kp inner rotor PI	0.1

Fig. 13 shows the output speed of the wheels with and without brake. The step torque tends to increase the speed of wheel 2 and in case of brake the tip speed is higher than the case without brake. In both cases because of the step torque the wheel 2 becomes asynchronous and its equilibrium point is now established only by the outer rotors mechanical coefficients. Wheel 1 remains synchronous and its equilibrium point is different with and without brake: this is due to the different speed of the poles' rotor which is now limited by the brake action.

Fig. 14 shows the poles rotor speed with and without brake. Clearly the speed exceeds the maximum allowed speed in the case without brakes, while with the brake the steady state speed approaches the speed limit. This means that the poles rotor is still coupled with the inner rotor, but the average torque transmitted to the outer rotor is zero. In this paper a brake PI controller is implemented in order to limit the poles over-speed to zero, but alternative solutions could be used.

In order to design the PI controller, the transfer function Y_{44} in (12) is needed. The zero of the PI can be designed in order to delete the pole with time constant $T = J_s/b_s$.

F. Loop With Road Transfer Function

When the overall system is considered, the wheel dynamics are governed by the vehicle dynamic equations [25]. These equations have to be implemented in order to obtain the entire closed loop. In this paper, a simplified model will be adopted for the wheel dynamic since the focus is the operation of the drivetrain rather than the whole vehicle. Several works in vehicle dynamics adopt the so called "Magic Formula", an empirical based equation introduced by [26] capable of modelling the force-slip curves. Although several expressions for the Magic Formula have been proposed, the basic law is:

$$F_x = DF_z \sin(C \arctan(B\sigma_x - E(B\sigma_x - \arctan(B\sigma_x)))) \tag{34}$$

where B,C,D,E are parameters that depend on the geometry and material of the tire and of the road. F_z is the vertical load on each tire and $\sigma_x = \frac{\omega R - v}{v}$ is the longitudinal slip where ω is the wheel speed and R is the wheel radius and v is the vehicle speed. Fig. 15 shows the reaction force as slip function for different vertical load conditions. As can be noted, the curves have a peak value and after this limit curve becomes unstable and the wheel starts to slip permanently.

In order to add the road transfer function, the slip is first computed from the actual wheel tangential speed. Since the whole vehicle dynamics is not included in this first simplified

This article has been accepted for publication in IEEE Transactions on Transportation Electrification. This is the author's version which has not been fully edited and content may change prior to final publication. Citation information: DOI 10.1109/TTE.2022.3208628

$$Y_{11}^{A}|_{s\to 0} = \frac{30P_o^2}{\pi(2b_oP_i^2 + b_iP_o^2)} \tag{20}$$

$$Y_{21}^{A}|_{s\to 0} = Y_{31}^{A}|_{s\to 0} = Y_{12}^{A}|_{s\to 0} = Y_{13}^{A}|_{s\to 0} = -\frac{30(P_iP_o)}{\pi(2b_oP_i^2 + b_iP_o^2)} \tag{21}$$

$$Y_{41}^{A}|_{s\to 0} = Y_{14}|_{s\to 0} = 0 \tag{22}$$

$$Y_{22}^{A}|_{s\to 0} = Y_{33}^{A}|_{s\to 0} = \frac{30(4\,P_i^4\,b_o + {P_o}^4\,b_i + P_i^2\,{P_o}^2\,b_i + 4\,P_i^2\,{P_o}^2\,b_o + P_i^2\,{P_o}^2\,b_s + 2\,P_i\,{P_o}^3\,b_i + 8\,P_i^3\,P_o\,b_o)}{\pi\left(2\,b_o\,P_i^2 + b_i\,{P_o}^2\right)\left(2\,P_i^2\,b_o + 2\,{P_o}^2\,b_o + {P_o}^2\,b_s + 4\,P_i\,P_o\,b_o\right)} \tag{23}$$

$$Y_{23}^{A}|_{s\to 0} = Y_{32}^{A}|_{s\to 0} = -\frac{30P_o^2(P_i^2b_i + P_o^2b_i - P_i^2b_s + 2P_iP_ob_i)}{\pi((2b_oP_i^2 + b_iP_o^2)(2P_i^2b_o + 2P_o^2b_o + P_o^2b_s + 4P_iP_ob_o))} \tag{24}$$

$$Y_{24}^{A}|_{s\to 0} = Y_{42}^{A}|_{s\to 0} = -Y_{34}^{A}|_{s\to 0} = -Y_{43}^{A}|_{s\to 0} = \frac{30P_o(P_i + P_o)}{\pi(2P_i^2b_o + 2P_o^2b_o + P_o^2b_s + 4P_iP_ob_o)} \tag{25}$$

$$Y_{44}^{A}|_{s\to 0} = \frac{30P_o^2}{\pi(2P_i^2b_o + 2P_o^2b_o + P_o^2b_s + 4P_iP_ob_o)} \tag{26}$$

$$Y_{11}^{B}|_{s\to 0} = \frac{30(P_i + P_o)^2}{\pi({P_i}^2\,b_i + 2\,{P_i}^2\,b_s + {P_o}^2\,b_i + 2\,P_i\,P_o\,b_i)} \tag{27}$$

$$Y_{21}^{B}|_{s\to 0} = Y_{31}^{B}|_{s\to 0} = Y_{12}^{B}|_{s\to 0} = Y_{13}^{B}|_{s\to 0} = \frac{30P_i(P_i + P_o)}{\pi({P_i}^2\,b_i + 2\,{P_i}^2\,b_s + {P_o}^2\,b_i + 2\,P_i\,P_o\,b_i)} \tag{28}$$

$$Y_{41}^{B}|_{s\to 0} = Y_{14}|_{s\to 0} = 0 \tag{29}$$

$$Y_{22}^{B}|_{s\to 0} = Y_{33}|_{s\to 0} = \frac{30{P_o}^4\,b_i + P_i^4\,b_o + P_i^2\,{P_o}^2\,b_i + 4\,P_i^2\,{P_o}^2\,b_s + P_i^2\,{P_o}^2\,b_o + 2\,P_i\,{P_o}^3\,b_i + 2\,P_i^3\,P_o\,b_o}{\pi(\left(P_i^2\,b_i + 2\,P_i^2\,b_s + {P_o}^2\,b_i + 2\,P_i\,P_o\,b_i\right)\left(P_i^2\,b_o + 2\,{P_o}^2\,b_s + {P_o}^2\,b_o + 2\,P_i\,P_o\,b_o\right))} \tag{30}$$

$$Y_{23}^{B}|_{s\to 0} = Y_{32}^{B}|_{s\to 0} = -\frac{30(P_i + P_o)^2\,\left(P_o^2\,b_i - P_i^2\,b_o\right)}{\pi\left(P_i^2\,b_i + 2\,P_i^2\,b_s + {P_o}^2\,b_i + 2\,P_i\,P_o\,b_i\right)\left(P_i^2\,b_o + 2\,{P_o}^2\,b_s + {P_o}^2\,b_o + 2\,P_i\,P_o\,b_o\right)} \tag{31}$$

$$Y_{24}^{B}|_{s\to 0} = Y_{42}^{B}|_{s\to 0} = -Y_{34}^{B}|_{s\to 0} = -Y_{43}^{B}|_{s\to 0} = \frac{30P_o\,\left(P_i + P_o\right)}{\pi(P_i^2\,b_o + 2\,{P_o}^2\,b_s + {P_o}^2\,b_o + 2\,P_i\,P_o\,b_o)} \tag{32}$$

$$Y_{44}^{B}|_{s\to 0} = \frac{30(P_i + P_o)^2}{\pi(P_i^2b_o + 2P_o^2b_s + P_o^2b_o + 2P_iP_ob_o)} \tag{33}$$

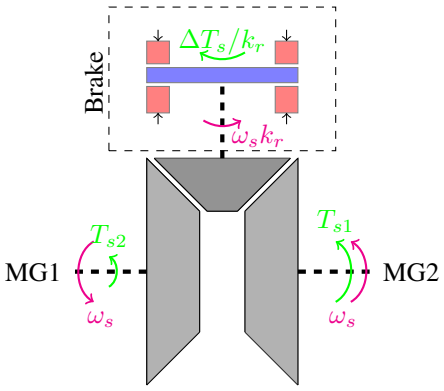

Fig. 11: Possible scheme of the torque inverter with a conventional brake and bevel gears. The gear ratio between the poles shaft of MG1 and MG2 is $G = -1$, while the gear ratio between input bevels and freewheel bevel is k_r.

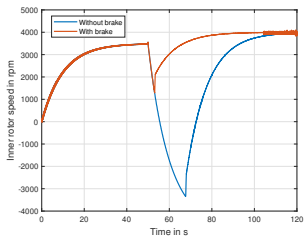

Fig. 12: Comparison between inner rotor speed ω_i with open loop with and without brake.

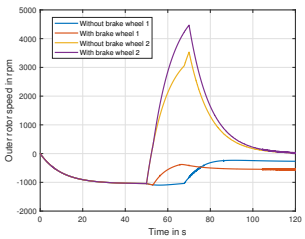

Fig. 13: Comparison between wheels speed ω_{o1} and ω_{o2} with and without brake.

model, the reference vehicle speed for the two wheels is considered as:

$$v_{ref} = \frac{1}{2}(\omega_{o1} + \omega_{o2})R_{wheel}\left(1 \pm \frac{w}{2R_c}\right) \tag{35}$$

This article has been accepted for publication in IEEE Transactions on Transportation Electrification. This is the author's version which has not been fully edited and content may change prior to final publication. Citation information: DOI 10.1109/TTE.2022.3208628

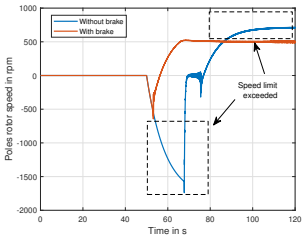

Fig. 14: Poles rotor speed ω_s with open loop: comparison with and without brake.

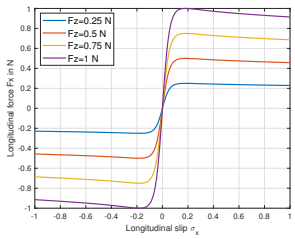

Fig. 15: Longitudinal force VS longitudinal slip VS vertical z force acting on the tire.

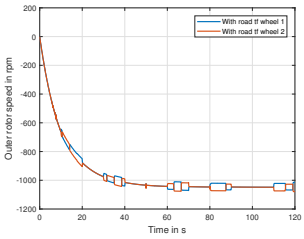

Fig. 17: Wheels speed ω_{o1} and ω_{o2} with the time dependent steering radius of Fig. 16.

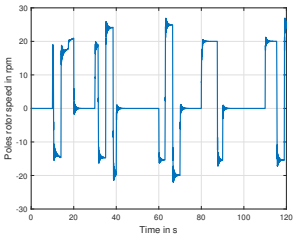

Fig. 18: Poles rotor speed ω_s with the time dependent steering radius shown in Fig. 16.

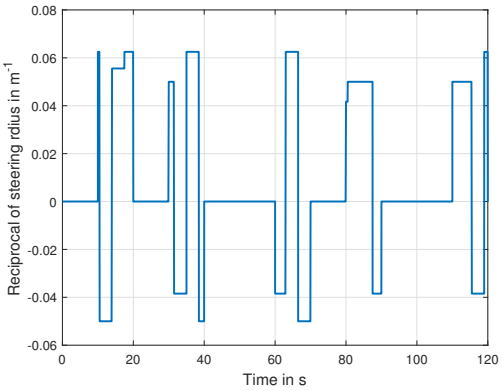

Fig. 16: Reciprocal of the steering radius adopted for the simulation. The radius r_c is positive when the drivetrain in Fig. 4 steers towards left.

TABLE III: Single magnetic gear geometrical parameters.

Parameter	Name	Value	
P_i	Inner pole pairs	5	-
P_o	Outer pole pairs	13	-
n_s	Iron poles	18	-
G	Gear ratio	3.6	-
tFe_{ext}	Outer rotor yoke thickness	8	mm
tFe_{int}	Inner rotor yoke thickness	8	mm
tPM_{ext}	Outer PM thickness	5	mm
tPM_{int}	Inner PM thickness	6.75	mm
$tAir_{ext}$	Outer airgap thickness	2	mm
$tAir_{int}$	Inner airgap thickness	2	mm
$tPoles$	Iron poles thickness	8.25	mm
L	Axial length	20	mm
δ_{Fe}	Iron lamination thickness	0.35	mm
α_{PM}^{in}	Inner PM angle	12	deg
α_{PM}^{out}	Outer PM angle	6.92	deg
nPM_{in}^{r}	Inner PM radial segments	3	-
nPM_{out}^{r}	Outer PM radial segments	2	-
nPM_{in}^{a}	Inner PM axial segments	2	-
nPM_{out}^{a}	Outer PM axial segments	2	-

where the higher reference speed is the one of the external wheel in the road curve. w is the wheels distance and R_c is the vehicle curvature radius. This vehicle model is approximated since the wheels just transmit force when the vehicle is steering. A more accurate vehicle model should consider that the vehicle is accelerated through the grip forces, but (34) also has to be changed since the slip calculation fails when the vehicle speed is close to zero.

The magnetic transmission is tested varying the steering radius and direction with a set of discrete values; for the simulation $R_{c-min} = 16$ m and $R_{c-max} = 26$ m. In Fig. 16 the reciprocal of the steering radius is plotted.

Fig. 17 shows the wheels rotor speed and in Fig. 18 the poles rotor speed is reported. The drivetrain remains synchronous and, as expected, the pole's rotor speed is 2 order of magnitude lower than the other rotors' speed.

V. Magnetic Differential Design

In this section, a specific magnetic differential is chosen and prototyped. The MDB configuration has been chosen since its gear ratio is higher than MDA for a given MG design (the manufacturing is also slightly easier). The rotational speeds are set to typical automotive ones, where internal combustion engines are normally in the range of $0-4$ krpms and the differential gear has a ratio around 4. The car gearbox reduction is supposed to be fixed to 1, which is normally the gear ratio for the 4th or 5th gear. The inner rotor nominal speed is set to $\omega_i = 3000$ rpm, and the differential gear ratio is set to $G_n = 3.6$. The design of the two MGs included in the MDB prototype has been carried out through the automatic procedure described in [27]. Through this method, the gear geometry has been optimized, in the multi-objective sense, as a trade-off between torque density and efficiency, while multi-physic constraints such as PMs demagnetization, thermal aspects and mechanical limits due to the materials have been accounted for. Among them, demagnetization turned out to be the most severe constraint for the design of these MGs, and an high intrinsic coercive field PM resulted from the optimization procedure (for a comprehensive overview of optimal MGs design versus PM grades the reader is referred to [28]). The geometrical parameters of the single optimal magnetic gear are reported in Tab. III, while the materials' main characteristics are summarized in Tab. IV.

After defining the prototype layout, each single magnetic gear is simulated first through standard 2D magneto-static (based on the vector potential $\mathbf{A}$) and 3D magneto-static finite element (FE) simulations (based on the magnetic scalar potential ψ), both performed with Comsol Multiphysics. This allows for evaluating static magnetic fields distributions and to asses the maximum torque of the differential and the torque ripple. After that, a 2D magneto-quasi-static FE simulation in time domain is performed to evaluate the losses in screws and PMs. This is used instead of a full 3D approach in order to limit the computational time and resources: the MG

This article has been accepted for publication in IEEE Transactions on Transportation Electrification. This is the author's version which has not been fully edited and content may change prior to final publication. Citation information: DOI 10.1109/TTE.2022.3208628

TABLE IV: Material characteristics of the two magnetic gears used in the prototype.

Parameter	Name	Value	
Fe	Ferromagnetic material	M400-50	-
ρ_{Fe}	Iron density	7700	$\frac{kg}{m^3}$
ρ_{e-Fe}	Electrical resistivity	45	$\mu\Omega cm$
λ	Thermal conductivity	28	$\frac{W}{mK}$
PM	Permanent magnets material	NdFeB 40SH	-
H_c	Coercive magnetic field	939	$\frac{kA}{m}$
H_i	Intrinsic magnetic field	1592	$\frac{A}{m}$
Br	Remanent flux density	1.26	T
T_{max}	Maximum operating temp.	150	$^\circ C$
PM_c	PM coating	Epoxy	-
ρ_{e-PM}	Electrical resistivity	150	$\mu\Omega cm$
PL	Thermoplastic	HD 3D PA 12	
ρ_{PL}	Thermoplastic density	1000	$\frac{kg}{m^3}$
σ_{PL}	Tensile strength	48	MPa
Screw	Screws material	Brass	-
ρ_s	Screws density	8500	$\frac{kg}{m^3}$
σ_s	Tensile strength	360	MPa
ρ_{e-s}	Electrical resistivity	6.3	$\mu\Omega cm$

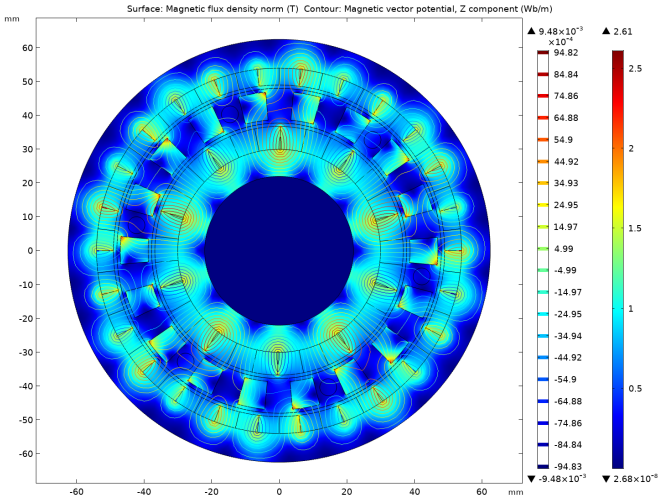

Fig. 19: Gear magnetic flux density and iso-A_z contour for arbitrary rotors positioning in a 2D simulation.

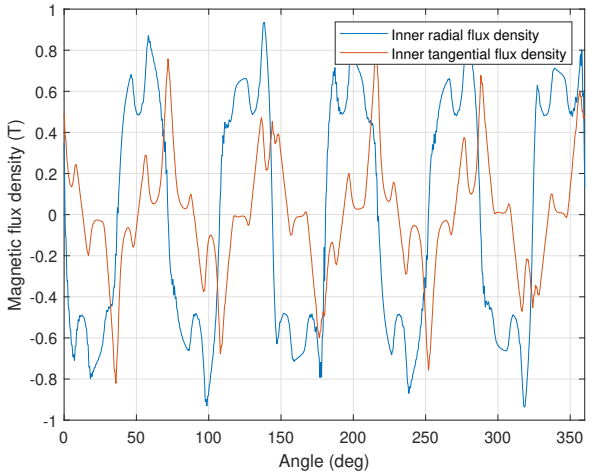

Fig. 20: Inner airgap magnetic flux density radial and azimuthal components in (T). The periodicity P_i is visible.

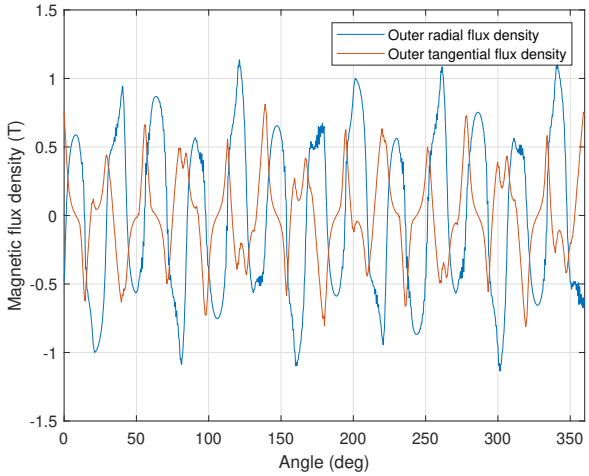

Fig. 21: Outer airgap magnetic flux density radial and azimuthal components in (T).The periodicity P_o is visible.

geometry is non-periodic thus the whole geometry needs to be modeled, leading to prohibitive efforts for a full 3D time domain simulation. As will be demonstrated later, this approach delivers satisfactorily accurate results.

In Fig. 19, the magnetic field norm is depicted while in Fig. 20 and Fig. 21 the radial and azimuthal magnetic flux densities for the inner and outer airgaps are depicted. The periodicities P_i and P_o can be clearly identified, while the modulation effect of the iron poles makes the waveforms non-sinusoidal. This is especially evident in the harmonic analysis of the radial fluxes in Tab. V, where the highest harmonics are shown. For example, in the inner airgap, the harmonic with order P_i is responsible for the torque transmission, while all the others induce eddy currents in the PMs and therefore contribute to power losses.

The simulated torques for an angular sweep of inner rotor positions and fixed iron poles and outer rotor are depicted in Fig. 22, while the maximum values are summarized in Tab. VI. The results are obtained with 2D and 3D magneto-static FE simulations, where the torque difference is due to the end effects of the axially short geometry ($L \ll D$): as shown in [29], [30], MGs suffer particularly from end effects if compared to conventional electrical machines, especially when torque evaluations are performed. This is due to the wide equivalent airgap between inner and outer rotor (which also accounts for the middle rotor slots) and the peculiar non-periodic MG magnetic structure, where some of the inner and outer magnets have opposite magnetization directions.

TABLE V: Harmonic analysis of the radial flux density of inner and outer rotors and normalization w.r.t. highest harmonic.

Inner airgap radial flux density			Outer airgap radial flux density		
Harmonic	Value (T)	p.u.	Harmonic	Value (T)	p.u.
5	0.387	1	5	0.111	0.28
13	0.0276	0.07	13	0.406	1
15	0.1	0.263	23	0.039	0.09
23	0.069	0.18	31	0.03	0.07
25	0.043	0.11	39	0.06	0.15

This article has been accepted for publication in IEEE Transactions on Transportation Electrification. This is the author's version which has not been fully edited and content may change prior to final publication. Citation information: DOI 10.1109/TTE.2022.3208628

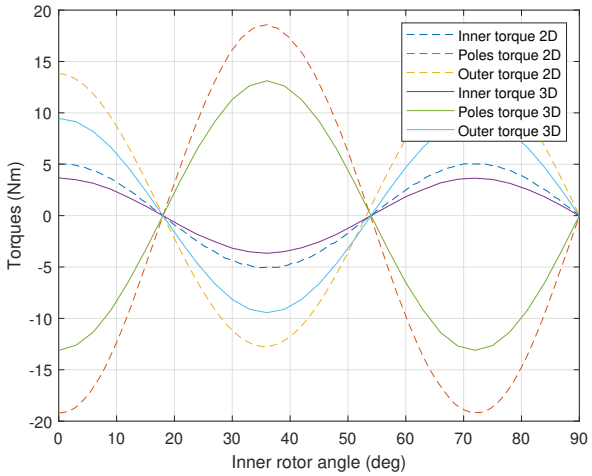

Fig. 22: Rotors torques (Nm) VS inner rotor angular position, poles and outer rotors fixed. Comparison between 2D and 3D magneto-static finite element simulation results.

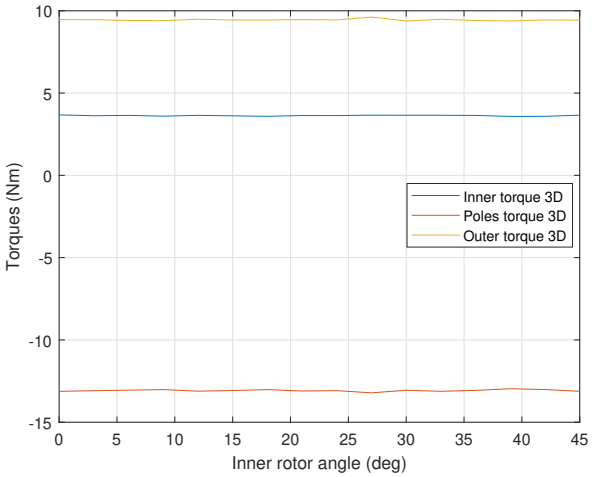

Fig. 23: Torque and ripples at the maximum load angle. The fractional gear ratio gives an almost negligible torque ripple.

The torque ripple is shown in Fig. 23 and is derived from angular sweeps of the inner and poles rotors with a relative position that results in the maximum achievable torque.

The eddy current losses in nonlaminated materials, i.e. PMs and screws, have been evaluated through 2D FE simulations in time domain, where additional constraints have been added on these solid domains to enforce the net current to be zero (otherwise in 2D a net current would flow). The $\mathbf{A}$ formulation adopted in the i^{th} solid domain with residual magnetization $\mathbf{B_r}$ is:

$$\begin{cases} \nabla \times (\nu \nabla \times \mathbf{A}) = -\sigma^i \dfrac{\partial \mathbf{A}}{\partial t} - \sigma^i \dfrac{V_i}{L}\mathbf{e_z} + \nabla \times (\nu \mathbf{B_r}) \\ \int_{S_i} J_z dS = \int_{S_i} \left(-\sigma^i \dfrac{\partial A_z}{\partial t} - \sigma_i \dfrac{V_i}{L} \right) dS = 0 \end{cases} \tag{36}$$

where $\mathbf{A} = A_z \mathbf{e_z}$ is the magnetic vector potential, ν is the magnetic reluctivity, J_z is the induced eddy current, σ_i is the PM or screw conductivity, S_i is the domain area, $-\sigma^i \frac{V_i}{L}\mathbf{e_z}$ is the additional current density term and V_i is the equivalent voltage drop across the i^{th} solid domain that ensures the net zero current property. The eddy current losses in PMs and screws are calculated through the integration $\int_{S_i} \frac{J_z^2}{\sigma_i} dS$. A different strategy to estimate the 3D PMs losses could be to introduce a fictitious PM conductivity as in [31].

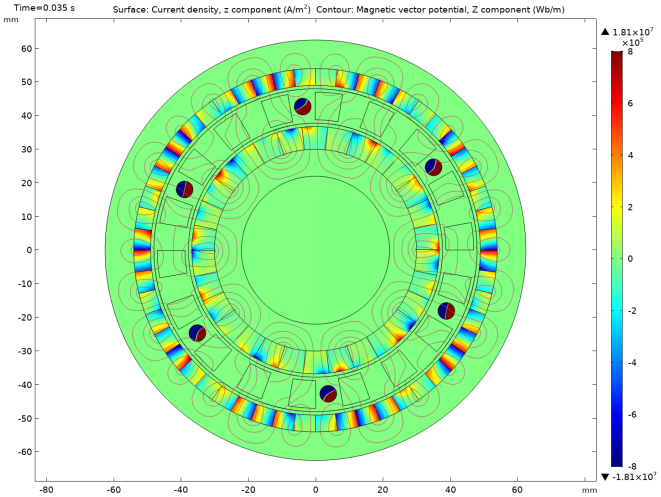

Fig. 24: Eddy currents snapshot from 2D time domain simulations along axial direction induced in permanent magnets at $\omega_i = 3000\ rpm$. The eddy current in each solid domain has zero integral according to (36).

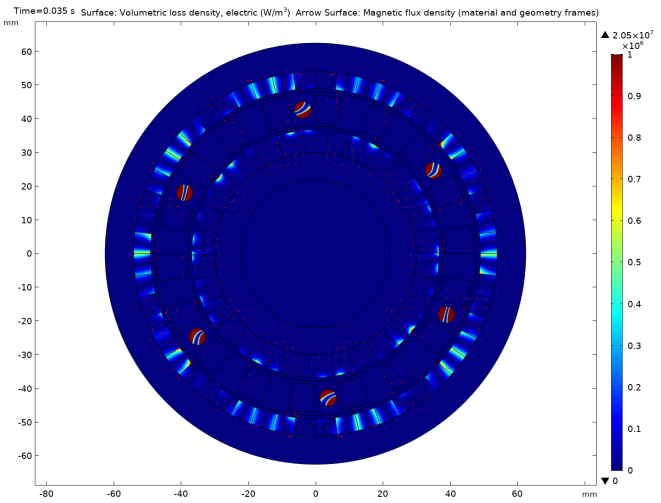

Fig. 25: Permanent magnet loss distribution snapshot at $\omega_i = 3000$ rpm from 2D time domain simulation. The loss contribution due to the asynchronous field with periodicity P_i is clearly visible on the outer rotor.

Figs. 24 and 25 show the induced eddy currents and the associated losses in the permanent magnet materials at inner rotor speed $\omega_i = 3000$ rpm and poles speed $\omega_s = 833.3$ rpm. A relevant induced current is developed in the poles rotor screws according to Fig. 24. In the outer magnets the trace of the asynchronous magnetic field with P_i periodicity due to the inner rotor is clearly visible: the inner rotor component generates a nil average torque and just contributes to losses.

TABLE VI: Single magnetic gear maximum rotor torques calculated with 2D and 3D magneto-static FE models.

Parameter	Name	Value	Unit
T_i^{2D}	Inner rotor max. torque	5.1	Nm
T_o^{2D}	Outer rotor max. torque	13	Nm
T_s^{2D}	Iron poles rotor max. torque	18.4	Nm
T_i^{3D}	Inner rotor max. torque	3.63	Nm
T_o^{3D}	Outer rotor max. torque	9.45	Nm
T_s^{3D}	Iron poles rotor max. torque	13.1	Nm
Δ_{2d-3d}	Delta between 2D and 3D	-29	%

TABLE VII: Magnetic differential prototype maximum speeds and mechanical couplings gear ratios.

Parameter	Name	Value	
ω_i^M	Maximum inner rotor speed	3000	rpm
ω_s^M	Maximum poles rotor speed	1000	rpm
ω_o^M	Maximum outer rotor speed	290	rpm
ω_{oo}^M	Maximum interconnection shaft speed	1450	rpm
ω_c^M	Maximum M2 rotor speed	1450	rpm
G_i	Mechanical ratio coupling source	1:1:1	-
G_o	Mechanical ratio coupling outer rotor	1:5	-
G_{oo}	Mechanical ratio coupling interconnection	1:1:-1	-

From the previous sections, the equation that relates the wheels speed in the MGB typology is:

$$\begin{cases} \omega_{s1} = \frac{P_o}{n_s}\omega_o + \frac{P_i}{n_s}\omega_i \\ \omega_{s2} = -\frac{P_o}{n_s}\omega_o + \frac{P_i}{n_s}\omega_i \end{cases} \tag{37}$$

In the maximum steering conditions formulated in Sec. II, the relation between the wheels speed is $\omega_{s1} = \Psi^{max}\omega_{s2}$, thus:

$$\omega_{s1} = \frac{P_o}{n_s}\omega_o + \frac{P_i}{n_s}\omega_i = \Psi^{max}\left(-\frac{P_o}{n_s}\omega_o + \frac{P_i}{n_s}\omega_i \right) \tag{38}$$

It is therefore possible to determine the maximum speed of the outer rotors and of the interconnection shaft:

$$\omega_o^M = \frac{P_i}{P_o}\frac{\Psi^{max}-1}{\Psi^{max}+1}\omega_i = \frac{5}{13}\frac{1.67-1}{1.67+1}3000 = 290 \text{ rpm} \tag{39}$$

The speed of the interconnected shaft ω_{oo} reads:

$$\omega_{oo}^M = \frac{P_i}{P_o}\frac{\Psi^{max}-1}{\Psi^{max}+1}\omega_i\frac{1}{G_o} = 290 \cdot 5 = 1450 \text{ rpm} \tag{40}$$

The nominal speeds of the prototype shafts are summarized in Tab. VII. In Fig. 26, a schematic representation of the MDB test rig is depicted.

VI. Motors Data and Electromagnetic Losses Estimation

The permanent magnets synchronous motors main parameters are summarized in Tab VIII. In this paper, only M1, M2 and M3 are used for loss and maximum torque measurement.

The electromagnetic losses in a magnetic gear are due to time-varying fluxes in soft and hard magnetic materials and in solid nonmagnetic materials. The power loss in PMs is $P_{PM} = L \cdot \int_{S_{PM}} \rho_{PM} \cdot J_z^2 dS$ and the power loss in solid screws is $P_s = L \cdot \int_{S_s} \rho_s \cdot J_z^2 dS$, in accordance to Sec. V, where the time domain formulation (36) is used.

In soft materials, the flux loci is rotational in the whole volume, thus the conventional Steinmetz approaches would provide unreliable results. The generalized Steinmetz approach

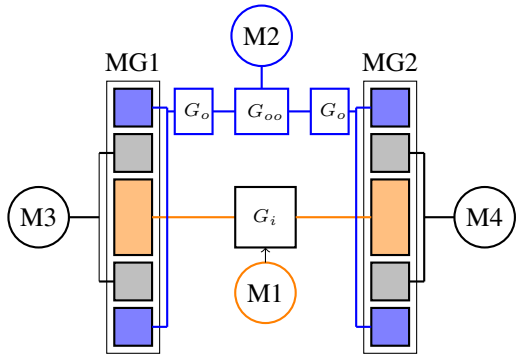

Fig. 26: Schematic connection of the MDB test rig. The motors M3 and M4 are the wheel loads. M1 is the high speed input motor, M2 is the auxiliary motor (see Fig. 36 for a comparison with the real prototype).

TABLE VIII: Prototype motors main parameters.

Parameter	Name	Value	
$Code$	Motor code	MTRI 140.50	
$Name$	Motor name in Fig. 26	M3 - M4	
n_s	Nominal speed	1500	rpm
T_n	Nominal torque	9.2	Nm
T_m	Maximum torque	25	Nm
J	Rotor inertia	4.2	kg cm^2
V_n	Nominal voltage	400	V
I_n	Nominal current	2.9	A
f_n	Nominal frequency	125 (10 poles)	Hz
$Code$	Motor code	MTRI 96.050.001	
$Name$	Motor name in Fig. 26	M1 - M2	
n_s	Nominal speed	3000	rpm
T_n	Nominal torque	5.2	Nm
T_m	Maximum torque	15	Nm
J	Rotor inertia	2.88	kg cm^2
V_n	Nominal voltage	400	V
I_n	Nominal current	3.5	A
f_n	Nominal frequency	200 (8 poles)	Hz

is the natural extension to non-sinusoidal waveforms [32], [33], and this method has been adopted for a first estimation of the gear efficiency despite the limited accuracy when DC biases are present.

According to the classical Steinmetz loss equation:

$$P_{Fe} = k \cdot f^{\alpha} B^{\beta} \tag{41}$$

the generalized specific loss is obtained:

$$P'_{Fe} = k' \cdot \left|\frac{dB}{dt}\right|^{\alpha} B^{\beta-\alpha} \quad \left(\frac{W}{Kg}\right) \tag{42}$$

where:

$$k' = \frac{k}{(2\pi)^{\alpha-1}\int_0^{2\pi} |\cos\theta|^{\alpha} |\sin\theta|^{\beta-\alpha} d\theta} \tag{43}$$

The values k, α and β are obtained through the fit of the material losses with the standard formulation (41).

The specific losses for the iron adopted for the yokes and poles are depicted in Fig. 27 for different values of polarization and frequencies. The fitting results in $k = 0.0011$, $\alpha = 1.688$, $\beta = 2.443$, $k' = 1.78 \cdot 10^{-4}$.

In Fig. 28 the 2D simulation result of the magnetic gear losses is presented: the inner rotor speed ranges between 0 to the nominal rotation speed $\omega_i = 3000$ rpm, and the load

This article has been accepted for publication in IEEE Transactions on Transportation Electrification. This is the author's version which has not been fully edited and content may change prior to final publication. Citation information: DOI 10.1109/TTE.2022.3208628

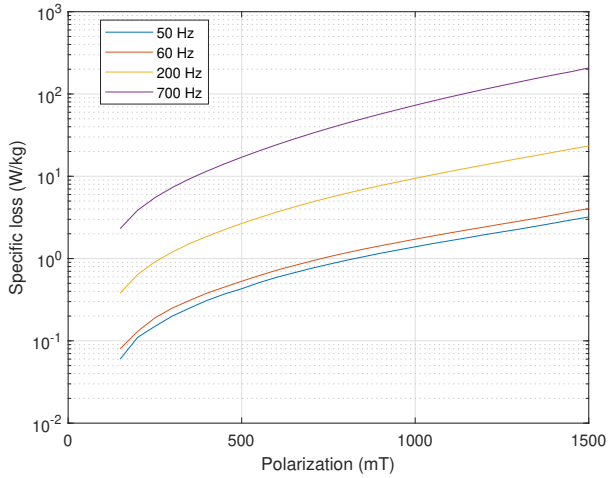

Fig. 27: Specific iron losses VS polarization at various frequencies.

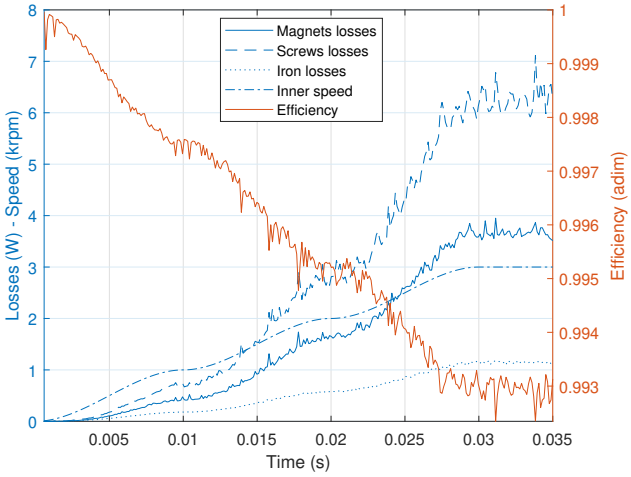

Fig. 28: Magnetic gear electromagnetic losses VS time for a continuously growing inner rotor speed from 0 to 3000 rpms (*Inner speed* in the legend). Losses and efficiency are computed at maximum torque capability from 0 to ω_i^M.

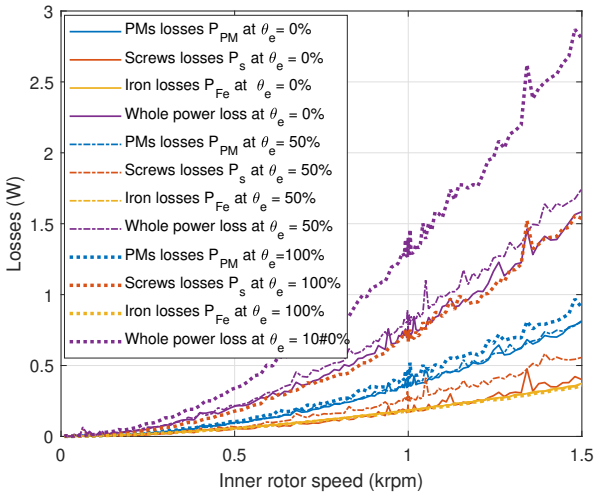

Fig. 29: Magnetic gear electromagnetic losses VS inner rotor speed for different load angles θ_e. The trend is always superlinear in accordance to the standard electrical machines.

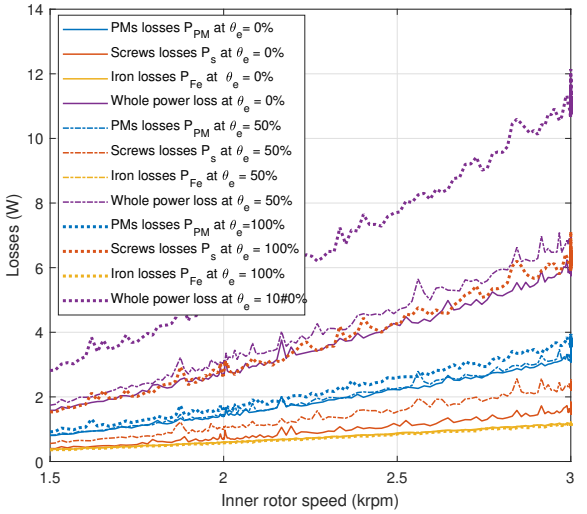

Fig. 30: Same quantities of Fig. 29 in the speed range $1.5-3$ krpm.

angle is the maximum one. As expected, the losses associated to eddy currents increase quadratically with the speed, while the iron losses grows sub-quadratically. A relevant loss contribution is given by the screws. Figs. 29 and 30 show the loss trend for different load angles, i.e. $\theta_e = 0$, $\theta_e = \pi/4$ and $\theta_e = \pi/2$. While the iron and PMs losses are independent on the load angle, the eddy losses inside the poles screws have a stronger dependence on the load angle, with a maximum when $\theta_e \to \pi/2$. This trend is confirmed in [34], where the efficiency map reaches the highest values at low speeds and are weakly dependent on the load angle.

VII. Damping and Inertia Estimation

In this section, the bearings losses and rotors inertia are analyzed. These parameters complete the set of data needed by the reader interested in modeling the dynamic responses of the system. The friction is related to several factors according to [35]. The most relevant are the lubricant type and temperature, the axial and radial bearing loads, the rotational speed. For the prototype two SKF spheres bearings models have been adopted, with code 6002 and 61816. The main bearings data have been summarized in tables IX and X. In Figs. 31, 32 the friction losses and power losses VS rotational speeds are shown for radial loads $kr = 10$ N and $kr = 100$ N, negligible axial load, default temperature of 70 $°C$.

The exact friction evaluation would require a coupled electromagnetic - mechanical model. Since the friction is rather low if compared with the nominal torque of the differential, a constant cautelative radial load of 100 N is assumed, and the

This article has been accepted for publication in IEEE Transactions on Transportation Electrification. This is the author's version which has not been fully edited and content may change prior to final publication. Citation information: DOI 10.1109/TTE.2022.3208628

TABLE IX: SKF 6002 bearing parameters.

Parameter	Name	Value	
d	Shaft diameter	15	mm
B	Bearing width	9	mm
m	Bearing mass	0.03	kg
v_{lim}	Speed limit	32	krpm
C_{100}	Static friction torque, 100 N	1	Nmm
b_{100}	Speed dependent interpolation, 100 N	0.0037	Nmm s/rad

TABLE X: SKF 61816 bearing parameters.

Parameter	Name	Value	
d	Shaft diameter	80	mm
B	Bearing width	10	mm
m	Bearing mass	0.15	kg
v_{lim}	Speed limit	8	krpm
C_{100}	Static friction torque, 100N	8.1	Nmm
b_{100}	Speed dependent interpolation, 100N	0.072	Nmm s/rad

linearized damping coefficients of each rotor is derived as:

$$\begin{cases} b_i = n_{6002} \cdot 0.0037 = 0.015 \text{ Nmm s/rad} \\ b_o = n_{61816} \cdot 0.0072 = 0.072 \text{ Nmm s/rad} \\ b_{s1} = b_{s2} = n_{61816} \cdot 0.072 = 0.288 \text{ Nmm s/rad} \end{cases} \quad (44)$$

where n stands for the number of bearings. The inertia estimation is more precise since its dependence is based only on the densities and geometry of the rotors. In Figs. 33 and 34 the inner rotor assembly and interconnected outer rotor assembly are shown, respectively.

VIII. Validation

In this section, the models for gear losses and the gear maximum input torque capability are validated through measurements. Fig. 35 represents simulated and measured losses for a single magnetic gear with no load on the output rotor (iron and bearings losses due to M3 are supposed to have a negligible effect on the load angle θ). In order to guarantee a fair comparison between the simulated losses and the measurements, the electromagnetic gear losses have been obtained by subtracting from the input power absorbed by M1 the iron and copper losses due to motor M1, the mechanical losses due to G_i, the mechanical and iron losses due to M3, and the bearings losses in the magnetic gear. By doing so, the electromagnetic losses of a single magnetic gear are found, and since the iron loss of M3 (which is the only contribution to the MG load) results in a load torque less then 5% of the gear nominal torque, thus the comparison with the simulated no-load condition holds. The measurements are shown from $\omega_i = 1500$ rpm in order to limit the numerical error obtained when small values are obtained by subtraction.

In Tab. XII, the differential input torque capability is validated. This measurement has been carried out by injecting in motors M3 and M4 a DC current $I = 5$ A ($I \simeq 1.25 \cdot \sqrt{2} I_n$) in two phases in order to block the wheels rotors and measuring the current of motor M1 with a fixed reference speed $\omega_r = 1$ rpm. The current grows with a triangular-like shape till the peak of Fig. 22, after that the inner rotor suddenly skips to the next stable equilibrium point. The differential torque is in good agreement with the 3D FE simulated one (retrieved

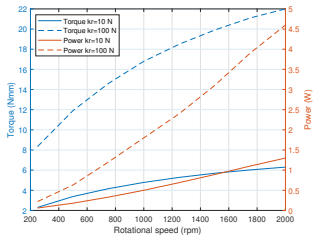

Fig. 31: Bearings 61816 theoretical friction torque and power losses with radial load $kr = 10$ N and $kr = 100$ N.

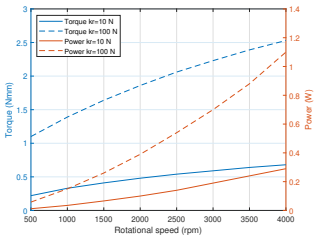

Fig. 32: Bearings 6002 theoretical friction torque and power losses with radial load $kr = 10$ N and $kr = 100$ N.

TABLE XI: Differential mechanical parameters.

Parameter	Name	Value	
b_i	Inner rotor damping	0.015	Nmm s/rad
b_o	Interconnection rotor damping	0.072	Nmm s/rad
b_s	Wheel rotor damping	0.288	Nmm s/rad
J_i	Inner rotor inertia	11.3	kg cm^2
J_o'	Intercon. rotor inertia (from MG)	313.3	kg cm^2
J_o''	Intercon. rotor inertia (from M2)	12.53	kg cm^2
$J_{s1},\ J_{s2}$	Wheel rotors inertia	12.5	kg cm^2

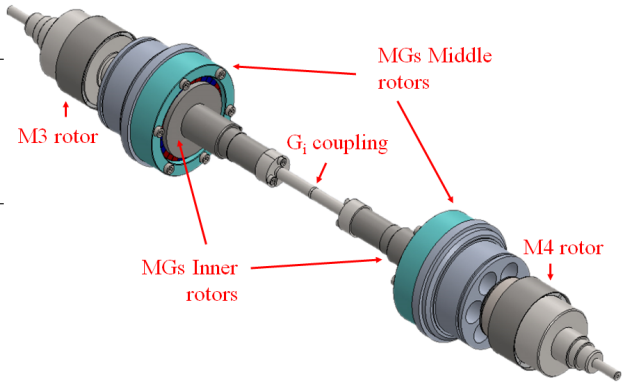

Fig. 33: Inner rotor (without traction motor) and poles rotors (without wheels) assembly for the evaluation of the inertia.

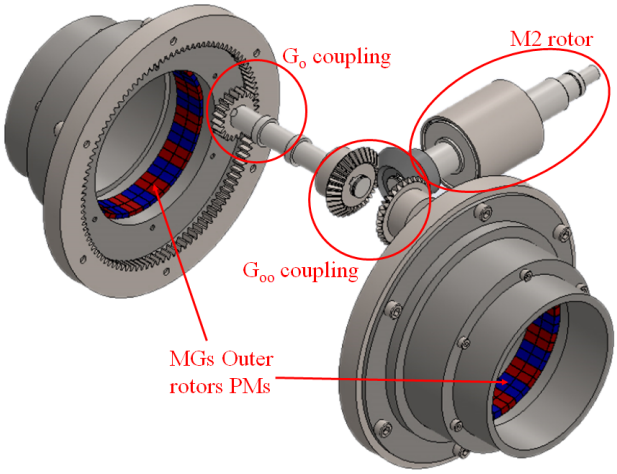

Fig. 34: Outer interconnected rotors assembly. The inertia seen from the gears side is different from the one seen by the control motor M2 side because of the coupling G_o.

This article has been accepted for publication in IEEE Transactions on Transportation Electrification. This is the author's version which has not been fully edited and content may change prior to final publication. Citation information: DOI 10.1109/TTE.2022.3208628

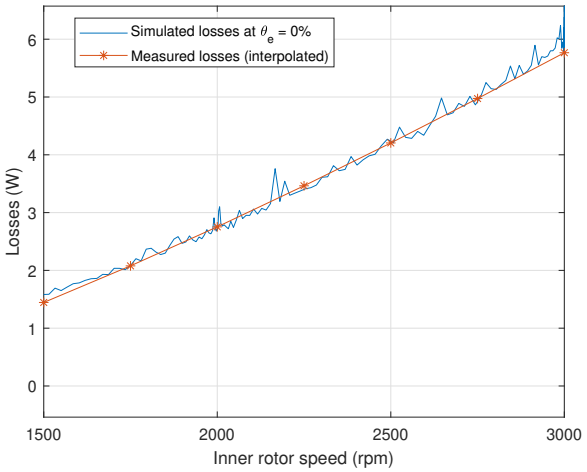

Fig. 35: Simulation VS measured losses of a single magnetic gear with no load ($\theta_e = 0$). The graph starts from $\omega_i = 1500$ rpm to limit the numerical error at low speeds.

TABLE XII: Validation of the differential maximum input torque $T_i^s = 2 \cdot T_i^{3D}$ (where T_i^{3D} is the 3D magneto-static torque in Tab. VI) VS measurement.

Parameter	Name	Value	Unit
$T_i^s = 2 \cdot T_i^{3D}$	Inner rotor max. FE torque 3D	7.26	Nm
T_i^m	Inner rotor max. measured torque	6.35	Nm
Δ	Difference	-12	%

from Tab. VI with a multiplying factor 2 since both MGs are connected), the differences can be justified by material and construction tolerances.

IX. Comments on Topology and Manufacturing

This section provides some comments regarding the class of magnetic differentials in general. On the one hand, mechanical differentials are a standard solution which is relatively easy to manufacture, but suffers from noise, vibrations, relatively low efficiency and needs maintenance. On the other, magnetic differentials can offer precious advantages, especially where maintenance is costly, but the system is more complex to manufacture since it has three rotors, even if multiple-rotor systems are quite diffused in mechanical systems (e.g. in planetary gear sets). Thus, there is not a clear advantage of one topology over the other, the best solution depends on the reliability level of the application and on the impact of each of the earlier cited factors. The MD could be used where high efficiency is required, where the presence of the lubrication oil could be problematic, when noise is a decisive factor or in the applications where particular layouts of the differential are requested.

From our experience in the manufacturing process of this device, MG inner and outer rotor are rather standard parts of conventional electrical machines, the challenging part is the middle rotor, since the iron poles are laminated and the mechanical structure should be designed in order to withstand electromagnetic and centrifugal forces. The 3D printing of the polymeric structure could be a good choice, but its feasibility depends on the size of the device and on the nominal torques of the middle rotor.

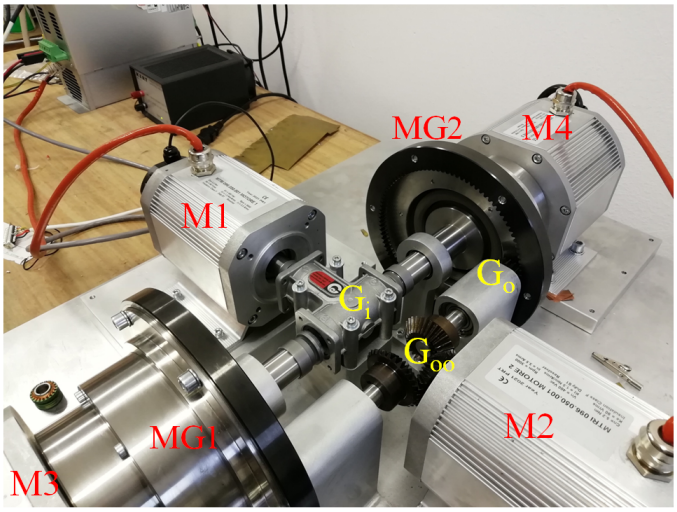

Fig. 36: Picture of the prototype. The motors labels are in accordance to the ones in Fig. 26: here the traction motor M1 is fed, while the other motors are in no load condition.

X. Conclusions

In this paper, magnetic differential devices are proposed as alternatives to conventional mechanical differentials. Two main topologies have been suggested and one of them has been prototyped. Detailed finite element analyses have been performed to estimate torque, torque ripples and losses of the differential and the results have been validated experimentally with very good agreement between models and measurements. The magnetic prototype has proven to achieve high levels of electromagnetic efficiency which grows with a superlinear trend typical of the electrical machines iron loss, thus its superiority over the mechanical device is especially marked at low speeds. The main differences with respect to mechanical differentials is the lower rotational stiffness (ideally the spur gears are infinitely stiff) and the power loss which is weakly dependent on the load (thus the highest efficiency is at full load). A future continuation of this work will focus on implementations of the control strategies of the magnetic differentials together with the full operation of the prototype with the true vehicle response emulation in steering conditions.

References

[1] V. Gleasman, "Differential gear mechanism," Nov. 1958, uS Patent 2,859,641.

[2] J. Juan de Santiago, H. Bernhoff, B. Ekergard, S. Eriksson, S. Ferhatovic, R. Waters, and M. Leijon, "Electrical motor drivelines in commercial all-electric vehicles: A review," *IEEE Transactions on Vehicular Technology*, vol. 61, no. 2, pp. 475–484, 2012.

[3] K. Atallah and D. Howe, "A novel high-performance magnetic gear," *IEEE Transactions on Magnetics*, vol. 37, no. 4, pp. 2844–2846, Jul 2001.

[4] A. Rotondale, M. Villani, and L. Castellini, "Analysis of high-performance magnetic gears for electric vehicle," in *2014 IEEE International Electric Vehicle Conference (IEVC)*, 2014, pp. 1–6.

[5] S. Pakdelian, N. W. Frank, and H. A. Toliyat, "Damper windings for the magnetic gear," in *2011 IEEE Energy Conversion Congress and Exposition*, 2011, pp. 3974–3981.

[6] K. Atallah, J. Wang, S. D. Calverley, and S. Duggan, "Design and operation of a magnetic continuously variable transmission," *IEEE Transactions on Industry Applications*, vol. 48, no. 4, pp. 1288–1295, jul 2012.

[7] K. T. Chau, D. Zhang, J. Z. Jiang, C. Liu, and Y. Zhang, "Design of a magnetic-geared outer-rotor permanent-magnet brushless motor for electric vehicles," *IEEE Transactions on Magnetics*, vol. 43, no. 6, pp. 2504–2506, June 2007.

[8] J. Wang, K. Atallah, and S. D. Carvley, "A magnetic continuously variable transmission device," *IEEE Transactions on Magnetics*, vol. 47, no. 10, pp. 2815–2818, Oct 2011.

[9] T. V. Frandsen, L. Mathe, N. I. Berg, R. K. Holm, T. N. Matzen, P. O. Rasmussen, and K. K. Jensen, "Motor integrated permanent magnet gear in a battery electrical vehicle," *IEEE Transactions on Industry Applications*, vol. 51, no. 2, pp. 1516–1525, 2015.

[10] P. Padmanathan and J. Z. Bird, "A continuously variable magnetic gear," in *2013 International Electric Machines Drives Conference*, May 2013, pp. 367–373.

[11] L. Jing, W. Tang, T. Wang, T. Ben, and R. Qu, "Performance analysis of magnetically geared permanent magnet brushless motor for hybrid electric vehicles," *IEEE Transactions on Transportation Electrification*, vol. 8, no. 2, pp. 2874–2883, 2022.

[12] W. Zhao and H. Zhang, "Coupling control strategy of force and displacement for electric differential power steering system of electric vehicle with motorized wheels," *IEEE Transactions on Vehicular Technology*, vol. 67, no. 9, pp. 8118–8128, 2018.

[13] C. Wang, J. Han, Z. Zhang, Y. Hua, and H. Gao, "Design and optimization analysis of coreless stator axial-flux permanent magnet in-wheel motor for unmanned ground vehicle," *IEEE Transactions on Transportation Electrification*, vol. 8, no. 1, pp. 1053–1062, 2022.

[14] Y.-C. Wu, M.-C. Tsai, and C.-T. Chan, "Creative mechanism design of magnetic gears integrated with continuously variable transmissions," *Advances in Mechanical Engineering*, vol. 10, no. 5, p. 1687814018772680, 2018.

[15] H. Rashidi and D. Pishdad, "Integrated multispeed magnetic gears: A novel approach to design of magnetic transmission systems," *IEEE Transactions on Magnetics*, vol. 51, no. 4, pp. 1–8, 2015.

[16] M. C. Gardner, M. Johnson, and H. A. Toliyat, "Analysis of high gear ratio capabilities for single-stage, series multistage, and compound differential coaxial magnetic gears," *IEEE Transactions on Energy Conversion*, vol. 34, no. 2, pp. 665–672, 2019.

[17] M. Filippini, P. Alotto, M. Repetto, E. Bonisoli, and V. Cirimele, "Differential and vehicle comprising such differential," *Patent: IT201800010648A1-WO2020110064A1*, 2018-2020.

[18] R. G. Montague, C. M. Bingham, and K. Atallah, "Magnetic gear dynamics for servo control," in *Melecon 2010 - 2010 15th IEEE Mediterranean Electrotechnical Conference*, April 2010, pp. 1192–1197.

[19] R. Montague, C. Bingham, and K. Atallah, "Servo control of magnetic gears," *IEEE/ASME Transactions on Mechatronics*, vol. 17, no. 2, pp. 269–278, April 2012.

[20] R. G. Montague, C. Bingham, and K. Atallah, "Magnetic gear pole-slip prevention using explicit model predictive control," *IEEE/ASME Transactions on Mechatronics*, vol. 18, no. 5, pp. 1535–1543, Oct 2013.

[21] M. Veneri and M. Massaro, "The effect of ackermann steering on the performance of race cars," *Vehicle System Dynamics*, vol. 59, no. 6, pp. 907–927, 2021.

[22] M. Johnson, A. Shapoury, P. Boghrat, M. Post, and H. A. Toliyat, "Analysis and development of an axial flux magnetic gear," in *2014 IEEE Energy Conversion Congress and Exposition (ECCE)*, 2014, pp. 5893–5900.

[23] P. M. Tlali, R.-J. Wang, and S. Gerber, "Magnetic gear technologies: A review," in *2014 International Conference on Electrical Machines (ICEM)*, 2014, pp. 544–550.

[24] H. Liu, L. Zhang, P. Wang, and H. Chen, "A real-time nmpc strategy for electric vehicle stability improvement combining torque vectoring with rear-wheel steering," *IEEE Transactions on Transportation Electrification*, pp. 1–1, 2022.

[25] M. Guiggiani, *Mechanics of the Wheel with Tire*. Dordrecht: Springer Netherlands, 2014, pp. 7–45.

[26] H. B. Pacejka and E. Bakker, "The magic formula tyre model," *Vehicle system dynamics*, vol. 21, no. S1, pp. 1–18, 1992.

[27] M. Filippini and P. Alotto, "Coaxial magnetic gear design and optimization," *IEEE Transactions on Industrial Electronics*, vol. 64, no. 12, pp. 9934–9942, 2017.

[28] M. C. Gardner, B. Praslicka, M. Johnson, and H. A. Toliyat, "Optimization of coaxial magnetic gear design and magnet material grade at different temperatures and gear ratios," *IEEE Transactions on Energy Conversion*, vol. 36, no. 3, pp. 2493–2501, 2021.

[29] M. C. Gardner, B. E. Jack, M. Johnson, and H. A. Toliyat, "Comparison of coaxial radial flux magnetic gears independently optimized for volume, cost, and mass," in *2017 IEEE International Electric Machines and Drives Conference (IEMDC)*, 2017, pp. 1–8.

[30] S. Gerber and R.-J. Wang, "Analysis of the end-effects in magnetic gears and magnetically geared machines," in *2014 International Conference on Electrical Machines (ICEM)*, 2014, pp. 396–402.

[31] S. Ruoho, T. Santa-Nokki, J. Kolehmainen, and A. Arkkio, "Modeling magnet length in 2-d finite-element analysis of electric machines," *IEEE Transactions on Magnetics*, vol. 45, no. 8, pp. 3114–3120, 2009.

[32] J. Li, T. Abdallah, and C. Sullivan, "Improved calculation of core loss with nonsinusoidal waveforms," in *Conference Record of the 2001 IEEE Industry Applications Conference. 36th IAS Annual Meeting (Cat. No.01CH37248)*, vol. 4, 2001, pp. 2203–2210 vol.4.

[33] A. Krings and J. Soulard, "Overview and comparison of iron loss models for electrical machines," *Journal of Electrical Engineering*, vol. 10, no. 3, pp. 8–8, 2010.

[34] M. C. Gardner, M. Johnson, and H. A. Toliyat, "Performance impacts of practical fabrication tradeoffs for a radial flux coaxial magnetic gear with halbach arrays and air cores," in *2019 IEEE Energy Conversion Congress and Exposition (ECCE)*, 2019, pp. 3129–3136.

[35] "Bearing friction, power loss and starting torque." [Online]. Available: https://www.skf.com/uk/products/rolling-bearings/principles-of-rolling-bearing-selection/bearing-selection-process/operating-temperature-and-speed/bearing-friction-power-loss-and-starting-torque